FULL PAPER

Electrodes

ADVANCED
FUNCTIONAL
MATERIALS

www.afm-journal.de

Improved Performance in FeF$_2$ Conversion Cathodes through Use of a Conductive 3D Scaffold and Al$_2$O$_3$ ALD Coating

Sanghyeon Kim, Jinyun Liu, Ke Sun, Junjie Wang, Shen J. Dillon, and Paul V. Braun*

FeF$_2$ is considered a promising conversion compound for the positive electrode in lithium-ion batteries due to its high thermodynamic reduction potential (2.66 V vs Li/Li$^+$) and high theoretical specific capacity (571 mA h g^{-1}). However, the sluggish reaction kinetics and rapid capacity decay caused by side reactions during cycling limit its practical application. Here, the fabrication of Ni-supported 3D Al$_2$O$_3$-coated FeF$_2$ electrodes is presented, and it is shown that these structured electrodes significantly overcome these limitations. The electrodes are prepared by iron electrodeposition on a Ni support, followed by a facile fluorination process and Al$_2$O$_3$ coating by atomic layer deposition. The 3D FeF$_2$ electrode delivers an initial discharge capacity of 380 mA h g^{-1} at a current density of 200 mA g^{-1} at room temperature. The 3D scaffold improves the reaction kinetics and enables a high specific capacity by providing an efficient electron pathway to the insulating FeF$_2$ and short Li diffusion lengths. The Al$_2$O$_3$ coating significantly improves the cycle life, probably by preventing side reactions through limiting direct electrode–electrolyte contact. The fabrication method presented here can also be applied for synthesis of other metal fluoride materials on different 3D conductive templates.

1. Introduction

Extensive research has been conducted on materials for lithium-ion batteries (LIBs) given the importance of energy storage for applications ranging from portable electronics to transportation,[1–3] and the fact that many key performance attributes, including the energy density of LIBs, are strongly determined by the electrode materials. While high-capacity anode materials such as Si, Sn, and Fe$_2$O$_3$ have been widely demonstrated,[4–6] development of high-capacity cathode materials has not been as successful. The most commonly used cathode materials are lithium transition metal oxides such as LiCoO$_2$.[1] Although they show good cycling stability, their specific capacities are limited by their storing Li$^+$ via intercalation, generally allowing a maximum of one Li to be accommodated per transition metal cation.[7] This has led to interest into conversion compound-based electrodes, which provide high specific capacities by utilizing all possible redox states of metal ions.[7,8] Among many conversion compounds, FeF$_2$ is one of the most promising candidates for positive electrodes due to its high thermodynamic reduction potential (2.66 V vs Li/Li$^+$), its high specific capacity (571 mA h g^{-1}), low cost, and low toxicity.[9–12] During discharge, FeF$_2$ is reduced with Li, forming a bicontinuous Fe network embedded in a LiF matrix. The reverse reaction occurs during charging (FeF$_2$ + 2Li ↔ Fe + 2LiF).[13,14] However, the poor electrical conductivity of FeF$_2$, combined with sluggish kinetics and large structural changes during cycling have resulted in an overall poor electrochemical performance, limiting the application of FeF$_2$.[7,15,16]

Carbon–FeF$_2$ nanocomposites have been evaluated as a route to address these issues.[11,17–20] Carbon enhances the conductivity of the electrode, and a nanostructured design can facilitate the conversion reaction kinetics owing to the increased surface area and decreased electron and ion diffusion lengths. However, high capacities could only be achieved at elevated temperature or low current densities, accompanied by rapid capacity decay.

Previous studies have suggested that capacity decay during cycling might be due to the incomplete reconversion of Fe and LiF to FeF$_2$.[13,21] Further capacity decay may result from metal dissolution into the electrolyte because newly formed Fe metal and LiF are exposed to the electrolyte each cycle.[19,22] Direct contact of cathodes with electrolyte, absent a stable solid electrolyte interphase, is generally unfavorable as it can cause many side reactions.[23] Therefore, an approach which protects the electrode surface from electrolyte during cycling needs to be considered.

S. Kim, Prof. J. Y. Liu, Dr. J. Wang, Prof. P. V. Braun
Frederick Seitz Materials Research Laboratory
Department of Materials Science and Engineering
Beckman Institute
University of Illinois at Urbana-Champaign
Urbana, IL 61801, USA
E-mail: pbraun@illinois.edu
Prof. J. Y. Liu
Institute of Intelligent Machines
Chinese Academy of Sciences
Hefei, Anhui 230031, P. R. China
Dr. K. Sun,[+] Prof. S. J. Dillon
Frederick Seitz Materials Research Laboratory
Department of Materials Science and Engineering
University of Illinois at Urbana-Champaign
Urbana, IL 61801, USA

[+]Present address: Brookhaven National Laboratory, 2 Center Street, Upton, New York, 11973

ADVANCED
SCIENCE NEWS
www.advancedsciencenews.com

ADVANCED
FUNCTIONAL
MATERIALS
www.afm-journal.de

Here, we describe the fabrication of a 3D conductive scaffold-supported Al_2O_3-coated FeF_2 electrode and demonstrate how the 3D metal scaffold and Al_2O_3 coating improve the electrochemical performance of FeF_2. The electrodes were prepared by electrodeposition and fluorination and coated with a thin layer of Al_2O_3 by atomic layer deposition (ALD). To the best of our knowledge, this is a first report describing the synthesis of 3D scaffolded metal fluorides. The porous electrode structure accommodates the large volume changes of the conversion compound during cycling. Relative to previous work, the reaction kinetics of FeF_2 with Li^+ were improved, likely because the active materials are in close contact with both a current collector and electrolyte. We observe enhanced capacity retention resulting from the Al_2O_3 ALD coating without suppression of electrode reaction kinetics.

2. Results and Discussions

Figure 1 shows a schematic of the 3D Ni@FeF_2 electrode fabrication. The Ni inverse opal serving as a 3D conductive scaffold was made via Ni electrodeposition through a polystyrene (PS) colloidal template. Fe metal nanoparticles were first deposited onto the Ni scaffold using pulsed electrodeposition. Pulse electrodeposition was then employed to deposit a conformal coating of Fe nanoparticles throughout Ni scaffold. The amount of Fe deposited was controlled by the number of pulses. The Fe nanoparticles were then selectively fluorinated into FeF_2 using an AgF_2 decomposition method. When AgF_2 is heated, it generates fluorine gas;[24] the F_2 gas then reacts with Fe forming FeF_2. Relative to other fluorination methods using fluorine gas or hydrofluoric acid, which are dangerous and require complicated experimental setups,[25–27] this method is facile and safe. Here, the method is optimized for the synthesis of FeF_2; however, the synthesis of other metal fluorides should also be possible by this route. Finally, ALD was used to coat the structure with 1–2 nm of Al_2O_3. We note that the surface roughness before and after ALD appears similar in scanning electron microscopy (SEM) (Figure S2, Supporting

Information) because the ALD coating layer is ultrathin (≈1.5 nm), and thus largely electron transparent. Since ALD was performed at low temperature (80 °C), there was no sintering of the underlying morphology.

Figure 2b shows that Fe metal particles were uniformly coated on the Ni inverse opal. An SEM image of the fluorinated Ni@Fe is presented in Figure 2c. A slight volume expansion of the active material was observed, probably due to the conversion of Fe to FeF_2. At room temperature (the Fe electroplating temperature), Fe does not react with Ni; however, we were concerned Fe and Ni might react during the fluorination process. To determine if this could occur, we refer to a previous study, which suggested the interatomic diffusivity in Fe/Ni multilayers is about 2.1×10^{-19} cm^2 s^{-1} at 300 °C.[28] Based on a simple diffusion calculation, interatomic diffusion at 300 °C for 1 h might yield a reacted layer about 0.5 nm thick. Since fluorination process was done at even lower temperature (250 °C) where the thickness of the reacted layer would be even less, we assume interatomic diffusion can be neglected. Also, a Ni signal has not been detected in the X-ray photoelectron spectroscopy (XPS) measurement, indicating Ni has not diffused through the Fe layer (the probe depth of XPS is at most 10 nm).

The 3D FeF_2@Ni retains its open porous structure with a pore size between voids of ≈200 nm after fluorination. One attribute of the inverse opal structure is its ability to accommodate the volume expansion of the active materials (about 50% for FeF_2)[25] during cycling and facilitate electrolyte infiltration into the electrode. The high-resolution transmission electron microscopy (HRTEM) image in Figure 2d displays lattice fringes of 0.33 nm, corresponding to the (1 1 0) *d*-spacing of tetragonal FeF_2. Selected area electron diffraction (Figure S3c, Supporting Information) shows the polycrystalline nature of FeF_2.

X-ray diffraction (XRD) was performed on Ni@Fe and Ni@Fe$_2$ samples. Metallic Fe was confirmed by XRD (**Figure 3**a). Figure 3b shows that all peaks in XRD pattern other than that of Ni and W match FeF_2. No metallic Fe was observed after fluorination, indicating that Fe was fully converted into
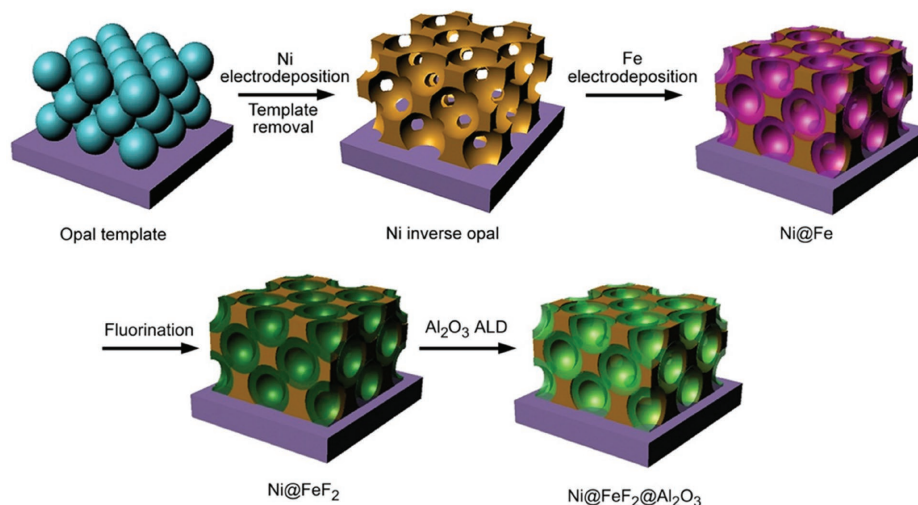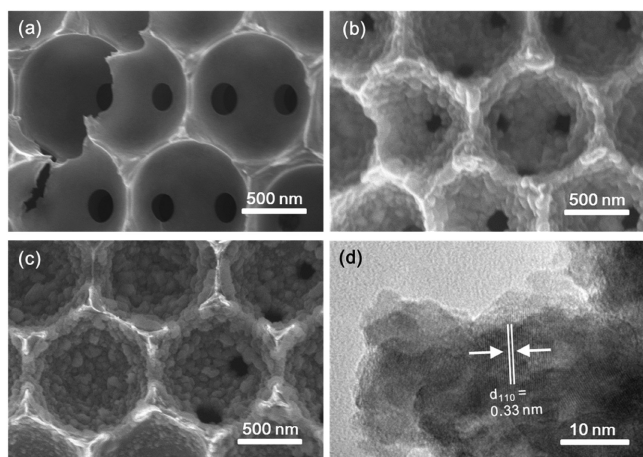

Figure 1. Schematic illustration of the 3D Ni@FeF_2@Al_2O_3 electrode fabrication process.

Figure 2. Cross-sectional SEM images of a) 3D Ni, b) 3D Ni@Fe, and c) Ni@FeF$_2$ inverse opals. d) HRTEM image of a small piece of the 3D Ni@FeF$_2$ electrode.

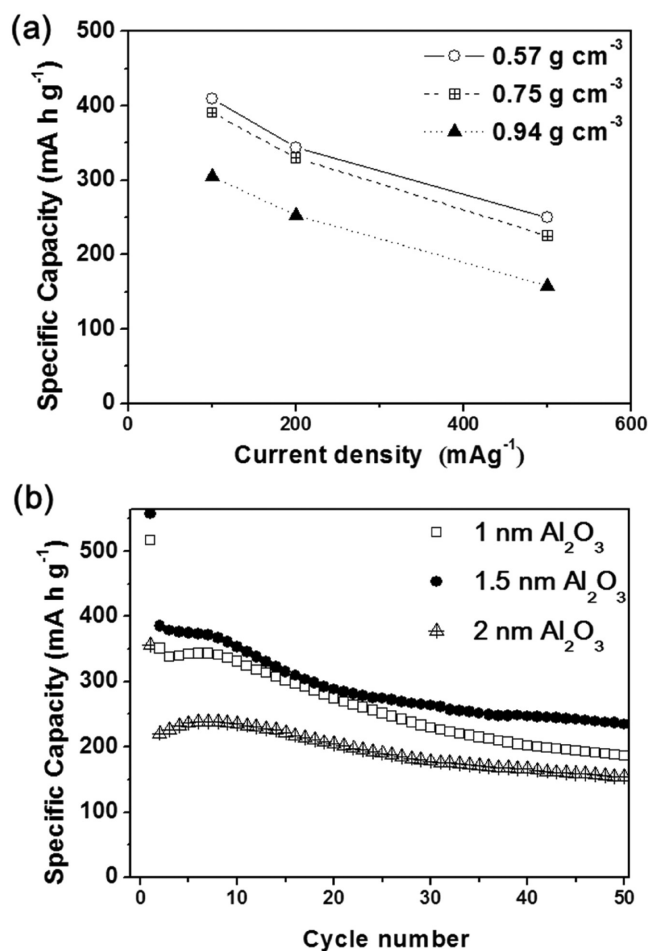FeF$_2$. The average FeF$_2$ grain size, calculated by the Scherrer equation,[29] is about 12 nm. XPS analysis (Figure 3c) also agrees with conversion of Fe into FeF$_2$. The Fe 2p XPS spectra measured from Fe and FeF$_2$ are shown in Figure 3c. The shift of the binding energy scale was corrected with respect to the C 1s peak (285 eV). The Fe 2p XPS of Fe is mainly composed of characteristic Fe^{3+} signal with two main peaks and satellite peaks. This is presumably because a few nanometers of outer surface of Fe are oxidized to Fe$_2$O$_3$. Fe 2p3/2 peak for metallic Fe is shown at around 707 eV.[14] After the fluorination, all satellite peaks of Fe^{3+} disappeared and Fe^{2+} peaks were formed.[14,30] The Fe 2p line shape matches that expected for FeF$_2$,[14] indicating that FeF$_2$ was converted from Fe. Also, no oxide formation was observed during the fluorination. Since Ni is covered by Fe, the possible oxide which can be formed primarily during fluorination would be iron oxide. No iron oxide phases were found in the TEM analysis (Figure 2d and Figure S3, Supporting Information). Moreover, In XPS, all satellite peaks of Fe^{3+} disappeared after the fluorination, indicating that any existing Fe$_2$O$_3$ was converted into FeF$_2$ (Figure 3c). The AgF$_2$ decomposition method is highly oxidizing but what we suspect is occurring is that the F$_2$ gas reacts preferentially with Fe over oxygen because of its high reactivity and because 250 °C is too low of a temperature for significant oxide formation especially considering the low gas pressure inside the reactor ($\approx 10^{-5}$ mbar, $\approx 10^{-6}$ Torr). Finally, to determine if nickel fluoride could be formed, a bare nickel inverse opal was treated using the same fluorination process. XRD (Figure S4a, Supporting Information) and energy dispersive spectroscopy (EDS) (Figure S4b, Supporting Information) indicate nickel fluoride was not formed.

The active material loading and ALD coating thickness that provided the best electrochemical performance were determined. First, the effect of FeF$_2$ loading on the electrochemical performance of the 3D Ni@FeF$_2$ electrode was examined. All variables, except FeF$_2$ loading, including electrode area and thickness, were identical across all samples. The specific capacities of three electrodes with different loadings at varying current densities are represented in **Figure 4**a.
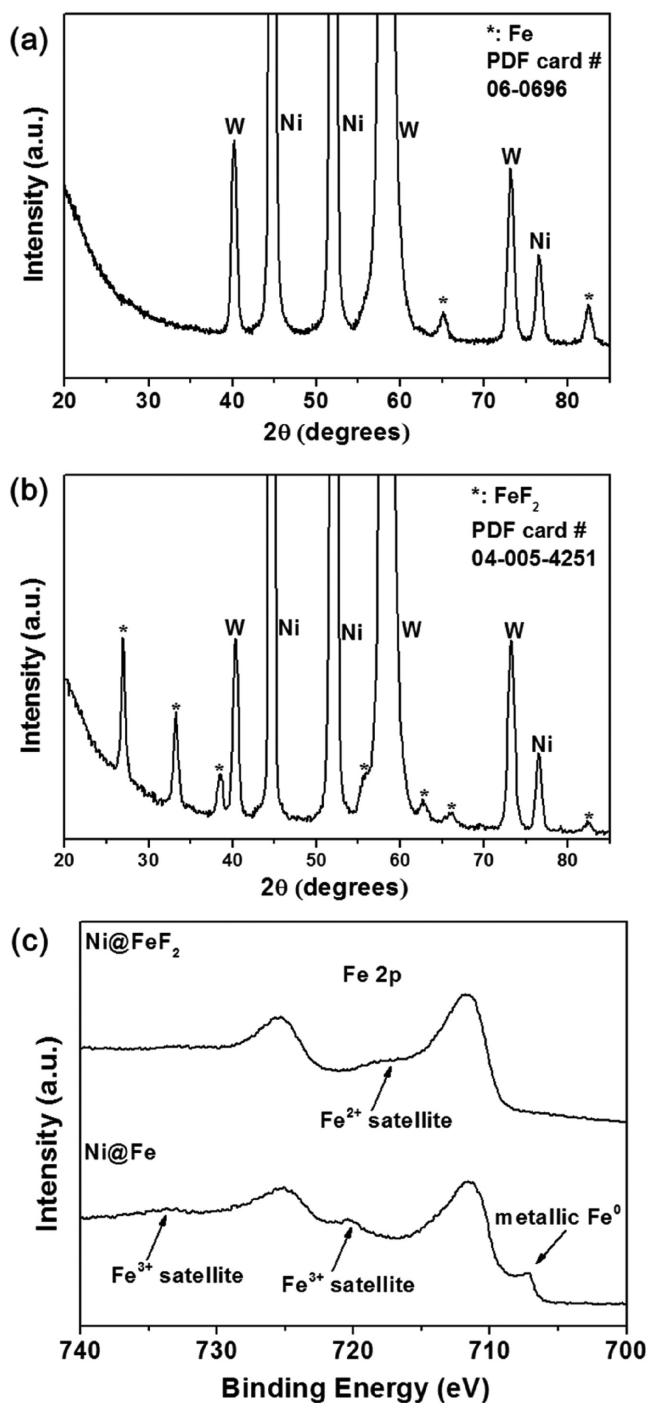
Figure 3. XRD and XPS before and after fluorination. XRD of a) a 3D Ni@Fe and b) 3D Ni@Fe@FeF$_2$. c) XPS spectra of Fe 2p region obtained from 3D Ni@Fe and Ni@FeF$_2$ samples.

The electrodes were cycled five times at each current density. As the FeF$_2$ loading increases, the specific capacity decreases. Higher FeF$_2$ loadings lead to longer electron and ion diffusion lengths, resulting in slow reaction kinetics. A higher active material loading also leads to narrower pores, which may reduce Li-ion transport ability due to limited electrolyte accessibility.[31,32] A significant capacity drop was observed in

ADVANCED
SCIENCE NEWS
www.advancedsciencenews.com

ADVANCED
FUNCTIONAL
MATERIALS
www.afm-journal.de

Figure 4. a) Specific capacity of Ni@FeF$_2$ electrodes with different active material loadings at various current densities. b) Specific capacities versus cycle number for 1-, 1.5-, and 2-nm-thick Al$_2$O$_3$-coated Ni@FeF$_2$ electrodes. All electrodes have the same active material loading (around 0.75 g cm^{-3}) and were cycled at 200 mA g^{-1}.

the electrode with a loading of 0.94 g cm^{-3}, so the electrode with a loading of 0.75 g cm^{-3} was chosen for most studies.

To avoid electrode degradation during cycling, an ultrathin (<2 nm) layer of Al$_2$O$_3$ was coated on Ni@FeF$_2$ by ALD; a common method for depositing ultrathin conformal coatings. Figure 4b shows how cycling stability changes with Al$_2$O$_3$ coating thickness. All electrodes were cycled at 200 mA g^{-1} and had the same FeF$_2$ loading (around 0.75 g cm^{-3}). As the Al$_2$O$_3$ thickness increases, cycling stability is improved. However, a large drop in initial capacity was observed for 2-nm-thick Al$_2$O$_3$ coatings, even though this thickness provided the most stable cycling behavior. This is perhaps because the thicker coating begins to significantly restrict Li diffusion.[33] On the basis of these results, 1.5 nm was determined to be a good Al$_2$O$_3$ coating thickness for our electrodes.

The electrochemical properties of FeF$_2$ electrodes were evaluated by galvanostatic discharge/charge tests at room temperature. **Figure 5**a shows the cycling performance of 3D Ni@FeF$_2$ electrodes with and without 1.5 nm Al$_2$O$_3$ coating at a current density of 200 mA g^{-1} over 100 cycles. 3D Ni@FeF$_2$ and

Ni@FeF$_2$@Al$_2$O$_3$ electrodes exhibit 557 and 473 mA h g^{-1} for the first discharge capacity, respectively. These correspond to 97.5% and 87.8% of the respective electrode theoretical value, indicating high active material utilization. After a few cycles, the uncoated electrode shows a similar capacity as the Al$_2$O$_3$-coated electrode. The capacity of the uncoated electrode then continues to decay more rapidly compared to the Al$_2$O$_3$-coated electrode. The Coulombic efficiency of the coated electrode exceeds that of the bare electrode after 22 cycles, gradually increases to 99% after 60 cycles and remains above 99% through 100 cycles. After 100 cycles, the capacity of the Al$_2$O$_3$-coated electrode is about 200 mA h g^{-1}. Considering the testing condition (200 mA g^{-1}, room temperature), this result is comparable or even better than the previous reported values for FeF$_2$ which were generally cycled at lower current densities (20–50 mA g^{-1}) and higher temperatures,[11,17,21,34] perhaps due to the combination of the highly conductive 3D metal scaffold and the ALD coating. Good electrical conductivity is important since FeF$_2$ is an electrical insulator. The porous nature of the electrode provides a path for Li-ion transport and provides a large surface area.[35] Furthermore, this electrode structure accommodates the large volume changes of FeF$_2$ (Figure S7, Supporting Information). While this is not easy to observe in SEM images, in Figure S9b (Supporting Information), the lithiated electrode appears denser, and the windows between the voids left by the colloids appear smaller. The structure can accommodate a 50% volume expansion, while any degradation of the structure due to the swelling during cycling was not observed. Previous research has shown that fast conversion reactions can be achieved when active material nanoparticles are in direct contact with a current collector,[36] as is the case in this work.

The Al$_2$O$_3$-coated FeF$_2$ second cycle discharge capacity is about 280 mA h cm^{-3}, higher than the previous reports for composite cathodes.[37,38] It is expected that even higher volumetric capacity 3D FeF$_2$ electrodes could be formed by optimizing the Ni inverse opal structure, something that is possible both through varying the diameter of the colloids forming the PS template and by Ni electropolishing.[35]

Figure 5b shows the initial two discharge–charge curves of the Ni@FeF$_2$@Al$_2$O$_3$ electrode, which are typical of FeF$_2$.[17,18] In the first discharge, a long plateau at around 1.6 V is observed which can be attributed to the reduction of FeF$_2$ to α-Fe and LiF.[13,18,39] After the first discharge, two stages are observed in the second discharge curve. The lithium uptake by FeF$_2$ at high potentials without conversion resulted in the steep slope to around 2.15 V; this effect is commonly observed in conversion compounds.[17,39] This lithium uptake may be due to interfacial lithium storage made possible by phase segregation through conversion and deconversion reactions,[7] and the formation of mixed or nonstoichiometric fluoride phases, which could have some capacity at higher voltages. The second slope represents the conversion reaction. The voltage plateau in the second discharge curve exhibits a higher reaction potential than that in first discharge curve perhaps due to the reduction of particle size after conversion reaction.[13] Improved reaction kinetics due to smaller nanoparticles after the first cycle reduces the overpotential, resulting in a higher reaction potential. dQ/dV curves were obtained by differentiating the charge/discharge voltage curves (Figure 5c). The dQ/dV curves show the reaction
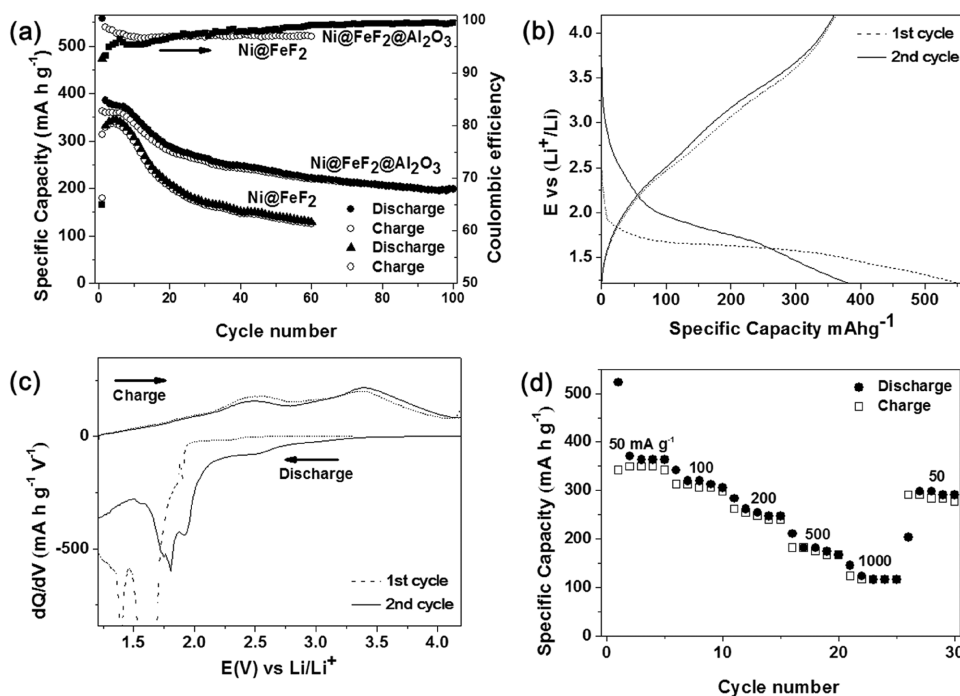
Figure 5. a) Cycling performance of 3D Ni@FeF$_2$@Al$_2$O$_3$ and Ni@FeF$_2$ at 200 mA g^{-1}. b) 1st and 2nd cycle discharge–charge curves of 3D Ni@FeF$_2$@Al$_2$O$_3$ at 200 mA g^{-1}. c) Differential capacity plot for cycles presented in Figure 4b. d) Rate performance of 3D Ni@FeF$_2$@Al$_2$O$_3$ electrodes. All electrodes have the same active material loading (around 0.75 g cm^{-3}).

peaks more clearly. Interestingly, two peaks were observed in the charge reaction curves, indicating that deconversion reaction consists of two steps, probably conversion and intercalation. The voltage hysteresis of Ni@FeF$_2$@Al$_2$O$_3$ in this work, defined as the voltage difference where half of charge capacity and discharge capacity were delivered, is about 1.2 V in contrast to the typical ≈1.7 V hysteresis for conventional slurry-cast FeF$_2$-based electrodes.[11,36]

The rate performance of the 3D Ni@FeF$_2$@Al$_2$O$_3$ electrode was evaluated by cycling the electrode at different current densities. When the current density increased from 50 to 100 and 200 mA g^{-1}, the electrode delivered 88% and 70% of its 50 mA g^{-1} capacity, respectively (Figure 5d). Even at 1000 mA g^{-1}, the electrode still delivered 32% capacity retention indicating that the slow reaction kinetics of conversion compounds can be enhanced by a 3D conductive scaffold. Moreover, when the rate returns from 1000 to 50 mA g^{-1}, about 83% of the 50 mA g^{-1} capacity was recovered.

To investigate the reason behind the different behavior of the bare and Al$_2$O$_3$-coated electrodes, XPS was performed on uncycled and cycled-ten-times bare electrodes, and ten-times-cycled Al$_2$O$_3$-coated electrodes (**Figure 6**). Duplicate experiments were performed for all samples and the same XPS results were obtained for all duplicate experiments. XPS spectra in Figure 6 were normalized for comparison. Carbon was detected on uncycled bare electrodes due to natural carbon contamination.[40] While the C 1s signal obtained from ten times cycled Al$_2$O$_3$-coated electrode is almost same as that obtained from the uncycled bare electrode, two new prominent peaks were observed in the ten-times-cycled bare electrode. After ten cycles, for the bare electrode, C 1s signals at 290.3 and 287 eV due

to C−F and C−O bonds, respectively,[41] were observed. Since no binder, carbon black, or LiPF$_6$ salt were used, FeF$_2$ and electrolyte should be the only sources for F and C. The C−F bond formation is thus evidence for a side reaction between FeF$_2$ and electrolyte. The C−O bond formation also indicates the electrolyte decomposition on the surface of the electrode. A similar trend was observed in the F 1s spectra (Figure 6b). The F 1s spectra obtained from uncycled bare electrodes and ten-times-cycled Al$_2$O$_3$-coated electrodes contain just one peak at 685.2 eV, which is a characteristics of F$^-$ in FeF$_2$.[40] However, C−F peaks were observed in the F 1s spectrum at 688.3 eV for the ten-times-cycled bare electrode.[42]

Unlike in the C 1s and F 1s spectra, peak position shifts or new peaks were not observed in Fe 2p spectra after cycling for all samples (Figure 6c); but, the Fe 2p intensity was much smaller for the bare versus the Al$_2$O$_3$-coated electrodes after ten cycles. Since XPS only detects, at most, the top 10 nm of a material, the reduced Fe 2p intensity from the bare electrode might be due to formation of an over layer or Fe loss by dissolution. Both these possibilities have been supported by previous studies which suggest that electrolyte decomposes on the surface of FeF$_2$, and metal ions in metal fluorides can become soluble in electrolyte during cycling.[19,21] In summary, based on the XPS data, we suspect that FeF$_2$ undergoes chemical degradation when cycled directly in contact with a carbonate-based electrolyte and the ALD coating prevents this side reaction by limiting contact of the electrode with the electrolyte.

To additionally evaluate the effect of the Al$_2$O$_3$ coating, differential capacity data for bare and Al$_2$O$_3$-coated electrodes for the 2nd, 5th, and 10th cycles (**Figure 7**) were examined to
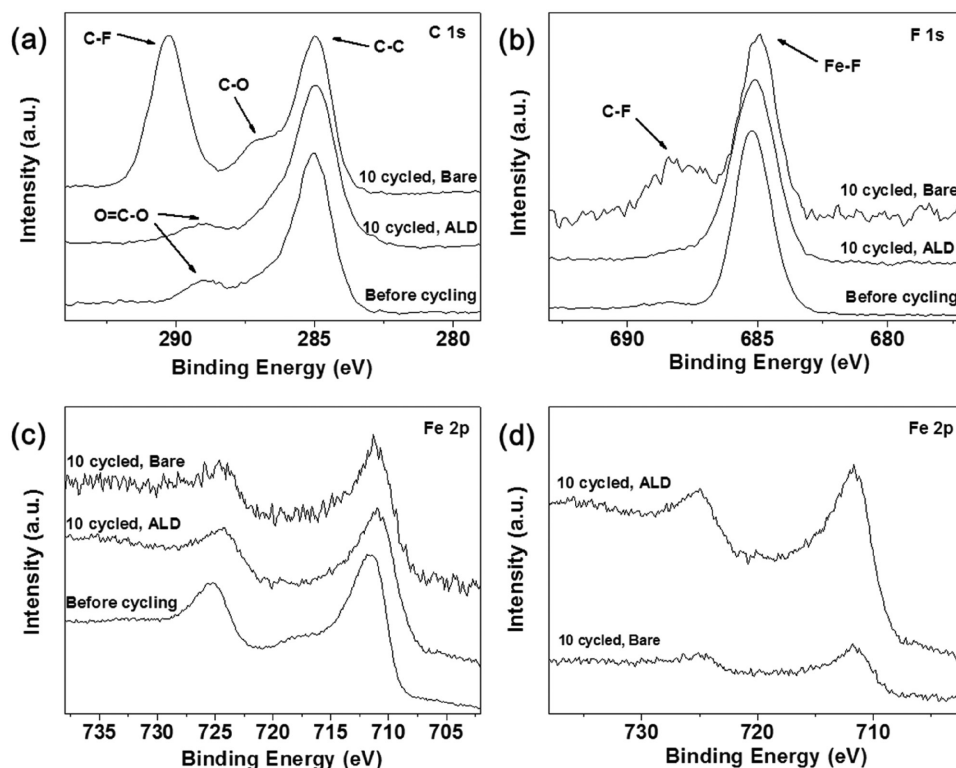
Figure 6. Normalized XPS spectra of a) C 1s, b) F 1s, and c) Fe 2p region obtained from uncycled and ten times cycled Ni@FeF$_2$ electrodes and an Ni@FeF$_2$@Al$_2$O$_3$ electrode cycled ten times. d) Original XPS spectra of Fe 2p region obtained from 3D Ni@FeF$_2$@Al$_2$O$_3$ and Ni@FeF$_2$ electrodes cycled ten times.

determine how surface reactions affect reaction kinetic. All oxidation and reduction peaks from the Al$_2$O$_3$-coated electrode overlap well from the 2nd to 10th cycle, indicating stable and reversible electrochemical reactions. However, the peak positions in the bare sample changes with cycling. In cathodic reaction, the conversion reaction peak moves toward lower voltage as cycling proceeds. This is due to increasing overpotential perhaps related to growth of an electrochemically inactive layer. This suggests that side reactions between the electrode and electrolyte affect the reaction kinetics. As described in the above, the deconversion reaction of FeF$_2$ consists of two steps, probably conversion and intercalation. Two oxidation peaks are clearly shown in the ALD-coated sample, which change little with cycling. In the bare sample, the first oxidation peak is disappearing with cycling, indicating the deconversion is incomplete. Therefore, the rapid capacity decay in bare samples can probably be attributed to incomplete deconversion lowering the utilization of active materials.[19,21,22] The ALD coating appears helpful to maintain the reversible electrochemical reaction.

The overall capacity behavior of Ni@FeF$_2$@Al$_2$O$_3$ electrode can be explained as follows (Figure 5a). We suspect that some SEI (solid electrolyte interface) forms forms on the surface of the Al$_2$O$_3$ ALD coating during the first few cycles, and perhaps there are also defects in the Al$_2$O$_3$ coating which become passivated with additional cycling. Initial contact between the electrolyte and any exposed FeF$_2$ leads to capacity decay, but capacity decay stabilizes with growth of the SEI layer.

3. Conclusion

Ni-supported 3D FeF$_2$ electrodes were fabricated by Fe metal electrodeposition combined with a facile fluorination method and Al$_2$O$_3$ ALD. The 3D scaffold enables a high specific capacity by providing an efficient electron pathway to the insulating FeF$_2$, and while there is still capacity fade in the coated electrode, the Al$_2$O$_3$ coating does improve both the Coulombic efficiency and capacity retention. The thin Al$_2$O$_3$ layer appears to reduce the degree of reaction between the active material and the electrolyte, improving the cycle life relative to that commonly observed in fluoride-based conversion compounds. This work demonstrates that a 3D conductive scaffold, coupled with a thin surface coating on the active material, reduces several of the drawbacks of an FeF$_2$-based electrode, specifically the typical sluggish reaction kinetics and rapid capacity fade. It is worth noting that the fabrication method presented here can be applied for synthesis of other metal fluoride materials on different types of 3D conductive scaffolds.

4. Experimental Section

Sample Preparation: A tungsten substrate (Sigma-Aldrich) was sonicated in concentrated ethanolic KOH for 30 min, rinsed with Millipore water, and dried. A PS suspension (0.2 wt%) was prepared by dispersing 1 µm PS spheres (Molecular Probes) in Millipore water. The tungsten substrate was vertically placed into vials filled with the PS suspension at 55 °C overnight. The substrate was taken out from
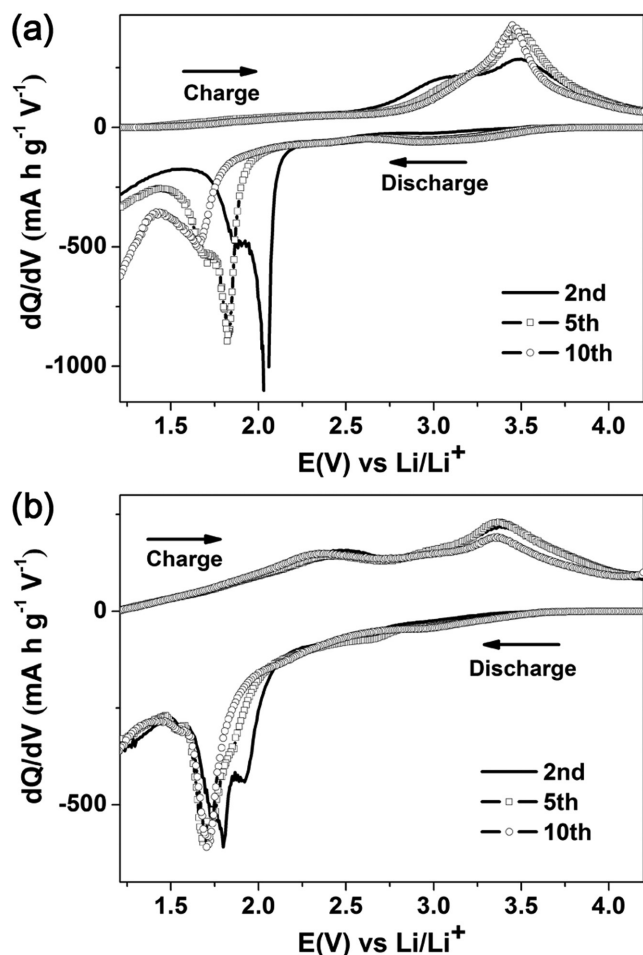
Figure 7. Differential capacity plot of a) Ni@FeF$_2$ and b) Ni@FeF$_2$@Al$_2$O$_3$ cycled at 200 mA g^{-1} for the 2nd, 5th, and 10th cycles.

equipped with an Oxford. energy-dispersive X-ray analyzer. The crystal structures were investigated by a Philips X'pert MRD (Materials Research Diffractometer) XRD using Cu K$_\alpha$ radiation (λ = 0.15418 nm). The crystal structures were also confirmed by electron diffraction in a JEOL 2100 Cryo TEM. XPS spectra were obtained with a Kratos Axis Ultra XPS system with a monochromatic Al K$_\alpha$ (1486.6 eV) source. The amount of active materials was determined by inductively coupled plasma (ICP-MS) analysis. For postmortem SEM and XPS analysis after cycling, electrodes were washed with dimethyl carbonate (DMC) multiple times and dried in the glove box prior to analysis.

Electrochemical Measurements: 1.0 M LiClO$_4$ in ethylene carbonate/DMC (1:1 by vol) was used as electrolyte and lithium foil was used as counter electrode for two-electrode cell. All cells were assembled in the glove box under Argon atmosphere. Galvanostatic discharge/charge tests were conducted on potentiostat (VMP3, Bio-Logic) in a jar cell over the range of 1.2–4.2 V.

Supporting Information

Supporting Information is available from the Wiley Online Library or from the author.

Acknowledgements

Conflict of Interest

The authors declare no conflict of interest.

the vials before the solution completely evaporated and subsequently annealed at 96 °C for 3 h to strengthen the adhesion between PS spheres and to increase the interconnect size between the PS spheres. Electrodeposition of Ni was performed by applying −1.5 mA cm^{-2} in a commercial Ni plating solution, with the sample as the working electrode and a nickel plate as a counter electrode. After the deposition, the sample was immersed into toluene to dissolve the PS template and Ni inverse opal was obtained. The final electrode thickness was typically about 6 μm.

Fe metal nanoparticles were electrodeposited on the Ni inverse opal by pulsed-voltage electrodeposition in a 0.375 M FeSO$_4$ solution. Platinum foil and an Ag/AgCl electrode saturated by 3 M NaCl (BASi Inc.) were used as the counter electrode and reference electrode, respectively. The cathodic pulses consisting of −0.8 V versus Ag/AgCl for 0.3 s and −1.6 V versus Ag/AgCl for 10 s were applied repeatedly. The amount of Fe metal deposited is proportional to the number of pulses applied. The sample was washed with Millipore water and ethanol and dried in vacuum oven. The sample was placed in a quartz reactor with Silver (II) fluoride (AgF$_2$, Sigma-Aldrich) to convert Fe metal into FeF$_2$. The sample and AgF$_2$ were spatially separated in the reactor and AgF$_2$ is not in direct contact with the electrode in the reactor (Figure S8, Supporting Information). Silver (II) fluoride was used as a fluorine precursor. The reactor was evacuated to 10^{-5} mbar and then heated to 250 °C for 1 h. The thin layer of Al$_2$O$_3$ was deposited on the sample in a Cambridge Nanotech ALD system at 80 °C. The growth rate was 0.9 nm per cycle.

Characterization: Sample morphologies were confirmed using a Hitachi S-4800 SEM. EDS was done using a Hitachi S-4700 SEM

Keywords

[1] M. Armand, J.-M. Tarascon, *Nature* **2008**, *451*, 652.
[2] J. B. Goodenough, *Acc. Chem. Res.* **2012**, *46*, 1053.
[3] J.-M. Tarascon, M. Armand, *Nature* **2001**, *414*, 359.
[4] H. Wu, G. Zheng, N. Liu, T. J. Carney, Y. Yang, Y. Cui, *Nano Lett.* **2012**, *12*, 904.
[5] G. Derrien, J. Hassoun, S. Panero, B. Scrosati, *Adv. Mater.* **2007**, *19*, 2336.
[6] X. Zhu, Y. Zhu, S. Murali, M. D. Stoller, R. S. Ruoff, *ACS Nano* **2011**, *5*, 3333.
[7] J. Cabana, L. Monconduit, D. Larcher, M. R. Palacin, *Adv. Mater.* **2010**, *22*, E170.
[8] P. Poizot, S. Laruelle, S. Grugeon, L. Dupont, J. Tarascon, *Nature* **2000**, *407*, 496.
[9] F. Badway, F. Cosandey, N. Pereira, G. Amatucci, *J. Electrochem. Soc.* **2003**, *150*, A1318.

[10] I. Plitz, F. Badway, J. Al-Sharab, A. DuPasquier, F. Cosandey, G. Amatucci, *J. Electrochem. Soc.* **2005**, *152*, A307.

[11] S. K. Martha, J. Nanda, H. Zhou, J. C. Idrobo, N. J. Dudney, S. Pannala, S. Dai, J. Wang, P. V. Braun, *RSC Adv.* **2014**, *4*, 6730.

[12] H. Li, P. Balaya, J. Maier, *J. Electrochem. Soc.* **2004**, *151*, A1878.

[13] F. Wang, R. Robert, N. A. Chernova, N. Pereira, F. Omenya, F. Badway, X. Hua, M. Ruotolo, R. Zhang, L. Wu, *J. Am. Chem. Soc.* **2011**, *133*, 18828.

[14] S. Rangan, R. Thorpe, R. A. Bartynski, M. Sina, F. Cosandey, O. Celik, D. D. Mastrogiovanni, *J. Phys. Chem. C* **2012**, *116*, 10498.

[15] L. Li, F. Meng, S. Jin, *Nano Lett.* **2012**, *12*, 6030.

[16] P. Liu, J. J. Vajo, J. S. Wang, W. Li, J. Liu, *J. Phys. Chem. C* **2012**, *116*, 6467.

[17] M. A. Reddy, B. Breitung, V. S. K. Chakravadhanula, C. Wall, M. Engel, C. Kübel, A. K. Powell, H. Hahn, M. Fichtner, *Adv. Energy Mater.* **2013**, *3*, 308.

[18] J. Zhou, D. Zhang, X. Zhang, H. Song, X. Chen, *ACS Appl. Mater. Interfaces* **2014**, *6*, 21223.

[19] W. Gu, A. Magasinski, B. Zdyrko, G. Yushin, *Adv. Energy Mater.* **2015**, *5*, 1401148.

[20] Y. Zhang, L. Wang, J. Li, L. Wen, X. He, *J. Alloys Compd.* **2014**, *606*, 226.

[21] M. Sina, R. Thorpe, S. Rangan, N. Pereira, R. A. Bartynski, G. G. Amatucci, F. Cosandey, *J. Phys. Chem. C* **2015**, *119*, 9762.

[22] X. Wang, W. Gu, J. T. Lee, N. Nitta, J. Benson, A. Magasinski, M. W. Schauer, G. Yushin, *Small* **2015**, *11*, 5164.

[23] X. Meng, X. Q. Yang, X. Sun, *Adv. Mater.* **2012**, *24*, 3589.

[24] W. Grochala, *J. Fluorine Chem.* **2008**, *129*, 82.

[25] Q. Chu, Z. Xing, J. Tian, X. Ren, A. M. Asiri, A. O. Al-Youbi, K. A. Alamry, X. Sun, *J. Power Sources* **2013**, *236*, 188.

[26] R. Ma, Z. Lu, C. Wang, H.-E. Wang, S. Yang, L. Xi, J. C. Chung, *Nanoscale* **2013**, *5*, 6338.

[27] H. Zhou, R. E. Ruther, J. Adcock, W. Zhou, S. Dai, J. Nanda, *ACS Nano* **2015**, *9*, 2530.

[28] J. Liu, K. Barmak, *J. Vac. Sci. Technol. A* **2015**, *33*, 021510.

[29] T. C. Vaimakis, C. S. Skordilis, P. J. Pomonis, *J. Colloid Interface Sci.* **1995**, *172*, 311.

[30] Y. Ma, G. Ji, J. Y. Lee, *J. Mater. Chem* **2011**, *21*, 13009.

[31] H. Zhang, P. V. Braun, *Nano Lett.* **2012**, *12*, 2778.

[32] J. Wang, H. Zhou, J. Nanda, P. V. Braun, *Chem Mater.* **2015**, *27*, 2803.

[33] Y. S. Jung, A. S. Cavanagh, A. C. Dillon, M. D. Groner, S. M. George, S.-H. Lee, *J. Electrochem Soc.* **2010**, *157*, A75.

[34] N. Pereira, F. Badway, M. Wartelsky, S. Gunn, G. Amatucci, *J. Electrochem. Soc.* **2009**, *156*, A407.

[35] H. Zhang, X. Yu, P. V. Braun, *Nat. Nanotechnol.* **2011**, *6*, 277.

[36] F. Wang, H.-C. Yu, M.-H. Chen, L. Wu, N. Pereira, K. Thornton, A. Van der Ven, Y. Zhu, G. G. Amatucci, J. Graetz, *Nat. Commun.* **2012**, *3*, 1201.

[37] C. Ban, Z. Wu, M. J. Kirkham, L. Chen, Y. S. Jung, E. A. Payzant, Y. Yan, M. S. Whittingham, A. C. Dillon, *Adv. Energy Mater.* **2011**, *1*, 58.

[38] M. Hara, H. Nakano, K. Dokko, S. Okuda, A. Kaeriyama, K. Kanamura, *J. Power Sources* **2009**, *189*, 485.

[39] N. Yamakawa, M. Jiang, B. Key, C. P. Grey, *J. Am. Chem. Soc.* **2009**, *131*, 10525.

[40] R. Thorpe, S. Rangan, R. Whitcomb, A. C. Basaran, T. Saerbeck, I. K. Schuller, R. A. Bartynski, *Phys. Chem. Chem. Phys.* **2015**, *17*, 15218.

[41] K. Bomben, J. Moulder, P. E. Sobol, W. Stickle, *Handbook of X-Ray Photoelectron Spectroscopy. A Reference Book of Standard Spectra for Identification and Interpretation of XPS Data*, Physical Electronics, Eden Prairie, MN **1995**.

[42] R. Dedryvere, S. Leroy, H. Martinez, F. Blanchard, D. Lemordant, D. Gonbeau, *J. Phys. Chem. B* **2006**, *110*, 12986.